

## Parallel domain decomposition method for finite element approximation of 3D steady state non-Newtonian fluids

Wen-Shin Shiu<sup>1,2</sup>, Feng-Nan Hwang<sup>1,\*,†</sup> and Xiao-Chuan Cai<sup>3</sup>

<sup>1</sup>*Department of Mathematics, National Central University, Zhongli District, Taoyuan City 32001, Taiwan*

<sup>2</sup>*Shenzhen Institutes of Advanced Technology, Chinese Academy of Sciences, Shenzhen, Guangdong 518055, China*

<sup>3</sup>*Department of Computer Science, University of Colorado, Boulder, CO 80309, USA*

### SUMMARY

We introduce a stabilized finite element method for the 3D non-Newtonian Navier–Stokes equations and a parallel domain decomposition method for solving the sparse system of nonlinear equations arising from the discretization. Non-Newtonian flow problems are, generally speaking, more challenging than Newtonian flows because the nonlinearities are not only in the convection term but also in the viscosity term, which depends on the shear rate. Many good iterative methods and preconditioning techniques that work well for the Newtonian flows do not work well for the non-Newtonian flows. We employ a Galerkin/least squares finite element method, with stabilization parameters adjusted to count the non-Newtonian effect, to discretize the equations, and the resulting highly nonlinear system of equations is solved by a Newton–Krylov–Schwarz algorithm. In this study, we apply the proposed method to some inelastic power-law fluid flows through the eccentric annuli with inner cylinder rotation and investigate the robustness of the method with respect to some physical parameters, including the power-law index and the Reynolds number ratios. We then report the superlinear speedup achieved by the domain decomposition algorithm on a computer with up to 512 processors. Copyright © 2015 John Wiley & Sons, Ltd.

Received 16 October 2014; Revised 17 January 2015; Accepted 23 February 2015

KEY WORDS: non-Newtonian fluids; stabilized finite element method; Newton–Krylov–Schwarz algorithm; parallel computing

### 1. INTRODUCTION

Many fluid flows in industrial and medical applications are non-Newtonian, for example, plastic polymers and blood flows in small arteries [1–3]. By definition, for non-Newtonian fluids, the relationship between the shear stress and the rate of deformation is nonlinear. Depending if the flow has memory, non-Newtonian fluids can be classified into two types [2, 4], time-independent or time-dependent fluids. In this paper, we focus on the time-independent fluid. The shear rate is determined only by the current value of shear stress. There are three major classes of time-independent flows. One of them is the pseudoplastic fluid, which exhibits the shear thinning behavior, that is, its viscosity decreases with increasing shear rate. Almost all polymer solutions and melts belong to this class. Examples are molten polyethylene, polypropylene, solution of carboxymethylcellulose in water, and so on. The velocity gradient tends to stretch out the polymer chains so that the fluid particles are able to move freely. The mathematical model commonly used for this class of fluids is the power-law or Ostwald Waele model. Opposite to the pseudoplastic fluid is the dilatant fluid, which possesses the shear-thickening property, that is, its viscosity increases with the increase of the shear rate. Only a

\*Correspondence to: Feng-Nan Hwang, Department of Mathematics, National Central University, Zhongli District, Taoyuan City 32001, Taiwan.

†E-mail: hwangf@math.ncu.edu.tw

few polymer solutions are dilatant. The third class is the viscoplastic fluid, which does not move unless the stress applied exceeds a critical value, such as the Bingham viscoplastic fluid.

In addition to the numerical difficulty arising from the incompressibility condition, the strong nonlinearities due to the convection term and the shear rate-dependent viscosity term make numerical solution of non-Newtonian flows more challenging than Newtonian flows. There are several research publications on the modeling and the simulation of non-Newtonian flows; see for examples [5–8] and their references. Some of the papers are devoted to the development of efficient iterative methods for non-Newtonian flows. To mention a few, Elias *et al.* [9, 10] employ a Newton–Krylov type algorithm to solve a 2D viscoplastic flow problem discretized with a streamline-upwind/Petrov–Galerkin/pressure-stabilizing/Petrov–Galerkin (SUPG/PSPG) stabilized finite element method. In the papers, they use Eisenstat and Walker’s adaptive stopping strategy for the forcing term [11] to avoid over-solving the Jacobian system and to enhance the robustness of inexact Newton method. Furthermore, in [9], an edge-by-edge block type preconditioner is proposed to accelerate the convergence of a Krylov subspace method in the 3D large-scale computation. In [12], a power-law non-Newtonian flow problem is considered. In the finite volume discretization, a pseudo-compressibility term is added to the conservation of mass equation, and the resulting time-dependent system is solved using a fully implicit time marching scheme together with Newton–Krylov type algorithm to obtain the steady-state solution. In addition, the performance of several block preconditioners, such as three-diagonal or five-diagonal blocks, where each block is approximated by an incomplete lower upper (ILU) decomposition is investigated. In [13, 14], the authors investigate a semi-implicit finite volume discretization of a viscoelastic fluid in the velocity–pressure–stress formulation. To solve the resulting algebraic system, they decouple the system as two sub-linear systems, including a generalized Stokes problem corresponding to the velocity and pressure variables, and a stress equation. To overcome the numerical difficulty due to the zero block in the saddle point problem, the authors propose to replace it with a scaled discrete Laplacian matrix so that an ILU(0) preconditioner or a multigrid preconditioner with standard smoothers can be used. In [15], Grinevich and Olshanskii study a Stokes-type problem with variable viscosity. A special block preconditioner based on the velocity diffusivity term and the pressure Schur complement for fully coupled system is introduced, and an analysis is also provided in the paper. In addition, Gwynllyw and Phillips [16] consider the time-dependent Stokes problem with the shear-thinning and pressure-thickening viscosity. The operator-splitting approach is employed to obtain a semi-positive definite linear system for the pressure variable and the discrete Helmholtz-type system for the velocity components. They investigate numerically the performance of two types of preconditioners based on the Schur complement and the Crank–Nicolson schemes for both the pressure and velocity systems.

In this paper, we introduce a finite element method for non-Newtonian fluids and a parallel coupled solver, which does not split the velocity and pressure variables, based on the Newton–Krylov–Schwarz (NKS) algorithm. The NKS algorithm consists of the following three key ingredients: (i) *an inexact Newton method* as a nonlinear solver [17]; (ii) *a Krylov subspace type method*, such as generalized minimal residual method (GMRES), as a Jacobian system solver; and (iii) *an overlapping Schwarz-type method* [18] as a preconditioner to accelerate the convergence of the linear solver. NKS has been successfully applied for a variety of applications in computational sciences and engineering, such as incompressible Newtonian flows, transonic flows, fluid–structure interaction problems [19–22], and flow control problems [23–25]. The aim of this study is to investigate the performance of NKS for non-Newtonian flows, in particular, its robustness with respect to the physical parameters and its parallel scalability.

As a test case, we study numerically some inelastic flows through the eccentric annuli with rotational inner cylinder. Although the geometry and flow condition are relatively simple, the physical structure of the fluid in the annuli is rather complicated because it consists of the entrance flow, the fully-developed flow, secondary flow, boundary layer, helical stream, and so on. Other similar problems have been intensively studied, for example, concentric annuli with or without inner cylinder rotation. Interested readers are referred to Appendix B in [26] for a comprehensive list of related works and Chin’s book [27] on this topic. One of the most important applications of annular flows is the drilling of oil wells. In these operations, the mud is pumped through the hollow drill shaft to the drill bit, where it enters the wellbore and returns under pressure as a helical flow to the well

surface. The primary functions of the mud are to carry rock cuttings to the surface, to lubricate the drill bit, and to control subsurface pressures. To reduce the computational cost, some simplifications are often used by researchers in this field; for example, if the annuli is long enough and there is no axial velocity, the 3D model can be reduced to 2D [10]. Another possible simplification is based on the assumption that the flow is fully developed, then the pressure gradient terms in the momentum equations can be computed with a small number of grid points in the axial direction [26, 28–31]. However, for more general situations, to fully understand the physics of annular flows, a full 3D model discretized on a fine 3D mesh is necessary and, hence, parallel computing becomes very important. The method to be studied in this paper is highly parallel and can be extended to other types of non-Newtonian flows.

The organization of this paper is as follows. In Section 2, we describe a mathematical model for 3D non-Newtonian flows, a finite element method to discretize the flow problem, and an NKS algorithm for solving the discretized problem. Some numerical results are presented in Section 3, including a grid independence test, a numerical validation of the algorithm using analytical solution, and a test case involving rotational eccentric annular flows. Parallel performance results are also given in Section 3. Some concluding remarks and possible future research directions are provided in Section 4.

## 2. FLOW MODELS, DISCRETIZATION, AND SOLUTION ALGORITHM

### 2.1. Problem statement

Consider the 3D steady-state incompressible non-Newtonian Navier–Stokes equations defined in  $\Omega \in \mathbb{R}^3$

$$\begin{cases} \rho(\mathbf{u} \cdot \nabla \mathbf{u}) - \nabla \cdot \boldsymbol{\sigma} = \mathbf{0} & \text{in } \Omega, \\ \nabla \cdot \mathbf{u} = \mathbf{0} & \text{in } \Omega, \\ \mathbf{u} = \mathbf{g} & \text{on } \Gamma_D, \\ \boldsymbol{\sigma} \cdot \mathbf{n} = \mathbf{0} & \text{on } \Gamma_N, \end{cases} \quad (1)$$

where  $\mathbf{u} = (u_1, u_2, u_3)^T$  is the velocity field;  $\rho$  is the fluid density, assumed to be a constant; and  $\boldsymbol{\sigma}$  is the Cauchy stress tensor defined as

$$\boldsymbol{\sigma} = -p\mathbf{I} + \boldsymbol{\tau},$$

where  $p$  is the pressure,  $\mathbf{I}$  is the identity tensor, and  $\boldsymbol{\tau}$  is the shear stress tensor. Here, we impose two types of boundary conditions on  $\partial\Omega = \Gamma_D \cup \Gamma_N$ .  $\Gamma_D$  is the Dirichlet-type boundary condition and  $\Gamma_N$  is the Neumann-type boundary condition. In the work, the generalized Newtonian model is employed, where the viscosity is a function of the second invariant of the deformation rate tensor [3, 32] and, unlike Newtonian flows, the relationship between the shear stress tensor and the deformation rate tensor is nonlinear, that is,

$$\boldsymbol{\tau} = 2\mu(I_2)\mathbf{D},$$

where  $\mu$  is the viscosity and  $I_2 = \frac{1}{2}\text{tr}(\mathbf{D}^2)$  is the second invariant of the deformation tensor. Here,  $\mathbf{D} = \frac{1}{2}[(\nabla \mathbf{u}) + (\nabla \mathbf{u})^T]$ , and  $\text{tr}$  denotes the trace of a second-order tensor. More specifically, the commonly used power-law is considered,

$$\mu(I_2) = \begin{cases} \mu_0 I_2^{(n-1)/2}, & \text{if } I_2 > \gamma_0, \\ \mu_0 \gamma_0^{(n-1)/2}, & \text{if } I_2 \leq \gamma_0, \end{cases} \quad (2)$$

where  $n$  is the power-law index. When  $n < 1$ , the flow is pseudoplastic. For example, nail polish, whipped cream, and ketchup are classified as this type of flows; on the other hand, when  $n > 1$ , the flow is called dilatant. Corn starch and sand in water belong to this type of fluids. Note that when

$n = 1$ , the power-law model reduces to be Newtonian. Other constants are  $\mu_0$ , the consistency index, and  $\gamma_0 > 0$ , the cutoff value for  $I_2$ . In the situation that  $I_2$  is close to zero, it is replaced by the cutoff value.

2.2. Galerkin/least squares finite element formulation

To discretize the incompressible generalized Newtonian Navier–Stokes equations (1), we employ the Galerkin/least squares (GLS) finite element method, which belongs to the class of stabilized finite element methods, which is popular for solving incompressible flow problems mainly due to the flexibility in choosing finite element basis functions for each variable (which does not need to satisfy the Ladyzhenskaya-Babuška-Breezi condition [33]), and more stable and accurate solution can be obtained for high Reynolds number flows. GLS is formulated as the traditional Galerkin finite element method plus the element-wise least-squares of the residual term. The associated stabilization scheme is originally designed for Newtonian flows and, in this work, we extend it to generalized Newtonian flows using the power-law model in a straightforward manner. Because stabilized finite element methods are not commonly used for non-Newtonian flows, we conduct a series of numerical experiments to validate our method in the numerical result section. We mention that a different stabilized finite element method based on SUPG/PSPG formulation is available in the literature for non-Newtonian flows [10].

Let  $\mathcal{T}^h = \{K\}$  be a conformal, quasi-uniform tetrahedron finite element mesh with the element diameter,  $h_K$ . Let  $V_h$  and  $P_h$  be a pair of piecewise linear continuous finite element spaces for the velocity and pressure, respectively

$$V_h = \left\{ \mathbf{v} \in (C^0(\Omega) \cap H^1(\Omega))^3 : \mathbf{v}|_K \in P_1(K)^3, K \in \mathcal{T}^h \right\}$$

and

$$P_h = \left\{ p \in C^0(\Omega) \cap L^2(\Omega) : p|_K \in P_1(K), K \in \mathcal{T}^h \right\}.$$

Here,  $C^0(\Omega)$  is the set of all continuous functions defined on  $\Omega$ ,  $L^2(\Omega)$ , and  $H^1(\Omega)$  are the standard notations with the usual meanings in the finite element literature [32–34]. The weighting and trial velocity function spaces  $V_h^0$  and  $V_h^g$  are

$$V_h^0 = \{ \mathbf{v} \in V_h : \mathbf{v} = 0 \text{ on } \Gamma_D \}$$

and

$$V_h^g = \{ \mathbf{v} \in V_h : \mathbf{v} = g \text{ on } \Gamma_N \}.$$

Similarly,  $P_h$  is used for both the weighting and trial pressure function spaces. The GLS finite element formulation for the incompressible generalized Newtonian Navier–Stokes equations (1) takes the following form: Find  $\mathbf{u}_h \in V_h^g$  and  $p_h \in P_h$ , such that

$$B(\mathbf{u}_h, p_h; \mathbf{v}, q) = 0 \quad \forall (\mathbf{v}, q) \in V_h^0 \times P_h \tag{3}$$

with

$$\begin{aligned} B(\mathbf{u}, p; \mathbf{v}, q) &= ((\rho \nabla \mathbf{u}) \cdot \mathbf{u}, \mathbf{v}) + (2\mu(I_2(\mathbf{u})) \mathbf{D}(\mathbf{u}), \mathbf{D}(\mathbf{v})) - (\nabla \cdot \mathbf{v}, p) - (\nabla \cdot \mathbf{u}, q) \\ &+ \sum_{K \in \mathcal{T}^h} ((\nabla \mathbf{u}) \cdot \mathbf{u} + \nabla p - 2\mu(I_2(\mathbf{u})) \nabla \cdot \mathbf{D}(\mathbf{u}), \tau_{GLS}((\nabla \mathbf{v}) \cdot \mathbf{v} + \nabla q - 2\mu(I_2(\mathbf{v})) \nabla \cdot \mathbf{D}(\mathbf{v})))_K \\ &+ (\nabla \cdot \mathbf{u}, \delta_{GLS} \nabla \cdot \mathbf{v}). \end{aligned}$$

We use the stabilization parameters  $\tau_{GLS}$  and  $\delta_{GLS}$  suggested in [34], with a modification of the element Reynolds number as

$$\tau_{GLS}(x, Re_K(x)) = \frac{h_K}{2|\mathbf{u}(x)|_2} \xi(Re_K(x)).$$

$$\delta_{GLS}(x, Re_K(x)) = \lambda |\mathbf{u}(x)|_2 h_K \xi(Re_K(x)), \text{ where } \lambda > 0.$$

Here,  $Re_K$  is an element Reynolds number defined as follows:

$$Re_K(x) = \frac{|\mathbf{u}(x)|_2 h_K}{12\mu(I_2(\mathbf{u}(x)))},$$

(For Newtonian flows, i.e.,  $n = 1$ ,  $\mu$  is a constant), and the function  $\xi$  is defined as

$$\xi(Re_K(x)) = \begin{cases} Re_K(x), & 0 \leq Re_K(x) < 1, \\ 1, & Re_K(x) \geq 1, \end{cases}$$

which distinguishes the locally convection-dominated flow as  $Re_K(x) \geq 1$  and the locally diffusion-dominated flow as  $0 \leq Re_K(x) < 1$ . Or, equivalently, the GLS formulation (3) can be written as a large, sparse, nonlinear algebraic system

$$F(x) = 0, \quad (4)$$

where the vector  $x$  corresponds to both the nodal velocity  $\mathbf{u}_h$  and pressure  $p_h$ . Note that the sources of nonlinearity are from the convection term and the nonlinear viscosity. These two terms are treated nonlinearly in this paper. This is different from the so-called semi-linear approach, in which the nonlinear terms are linearized using the approximate solution obtained from the previous iteration.

### 2.3. Newton–Krylov–Schwarz algorithm

We employ an NKS algorithm for solving large nonlinear systems of equations (4), which is described as follows. Let  $x^{(0)}$  be a given initial guess and assume  $x^{(k)}$  is the current approximation of  $x$ . Then a new approximation  $x^{(k+1)}$  can be computed by the following steps:

**Step 1:** Find a Newton direction  $s^{(k)}$  by solving the following preconditioned Jacobian system approximately by a Krylov subspace method, such as GMRES [35],

$$J_k s^{(k)} = -F(x^{(k)}), \text{ with } s^{(k)} = M_k^{-1} y, \quad (5)$$

where  $J_k$  is Jacobian of  $F$  evaluated at  $x^{(k)}$  and  $M_k^{-1}$  is the right additive Schwarz preconditioner.

**Step 2:** Obtain the new approximation  $x^{(k+1)} = x^{(k)} + \lambda^{(k)} s^{(k)}$ , where  $\lambda^{(k)} \in (0, 1]$  is a damping parameter.

In NKS, the accuracy of the solution to the Jacobian systems (5) is controlled by the parameter,  $\eta_k$ , to force the condition

$$\|F(x^{(k)}) + F'(x^{(k)})s^{(k)}\|_2 \leq \eta_k \|F(x^{(k)})\|_2$$

to be satisfied.  $\eta_k$  is often referred to as the forcing term. If  $\eta_k$  is small enough, the algorithm reduces to the exact Newton algorithm. In our implementation, the Jacobian matrix is constructed approximately, more precisely speaking, the components corresponding to the pressure gradient; the diffusive and convective terms in the Galerkin formulation are evaluated analytically. The terms corresponding to the partial derivatives of the nonlinear viscosity in the diffusive term with respect to the spatial variables are ignored because they are small relative to the other terms. All other terms involving the stabilization parameters are computed approximately by using a multicolored first-order forward finite difference scheme [36, 37]. The step length,  $\lambda^{(k)} \in [\lambda_{\min}, \lambda_{\max}] \subset (0, 1]$ , in Step 2 is selected so that

$$f(x^{(k)} + \lambda^{(k)} s^{(k)}) \leq f(x^{(k)}) + \alpha \lambda^{(k)} \nabla f(x^{(k)})^T s^{(k)},$$

where the two parameters  $\lambda_{\min}$  and  $\lambda_{\max}$  act as safeguards, which are required for strong global convergence; the merit function  $f$  is defined as  $\|F(x)\|_2^2/2$ ; and the parameter  $\alpha$  is used to assure that the reduction of  $f$  is sufficient. Here, a cubic linesearch technique [17] is employed to determine the step length,  $\lambda^{(k)}$ .

To define a parallel Schwarz preconditioner, we partition the finite element mesh  $\mathcal{T}^h$  introduced in the previous section. Let  $\{\Omega_i^h, i = 1, \dots, N\}$  be a non-overlapping subdomain partition whose union covers the entire domain  $\Omega$  and its mesh  $\mathcal{T}^h$ . Figures 1 and 2 show samples of 3D finite element mesh and its partition into non-overlapping submeshes. We denote  $\mathcal{T}_i^h$  as the collection of mesh points in  $\Omega_i^h$ . To obtain overlapping subdomains, we expand each subdomain  $\Omega_i^h$  to a larger subdomain  $\Omega_i^{h,\delta}$  with the boundary  $\partial\Omega_i^{h,\delta}$ . Here,  $\delta$  is an integer indicating the level of overlap. We assume that  $\partial\Omega_i^{h,\delta}$  does not cut any elements of  $\mathcal{T}^h$ . Similarly, we denote  $\mathcal{T}_i^{h,\delta}$  as the collection of mesh points in  $\Omega_i^{h,\delta}$ .

Now, we define the subdomain velocity space as

$$V_h^i = \left\{ v_h \in V_h \cap \left( H^1 \left( \Omega_i^{h,\delta} \right) \right)^3 : v_h = 0 \text{ on } \partial\Omega_i^{h,\delta} \right\}$$

and the subdomain pressure space as

$$P_h^i = \left\{ p_h \in P_h \cap L^2 \left( \Omega_i^{h,\delta} \right) : p_h = 0 \text{ on } \partial\Omega_i^{h,\delta} \setminus \Gamma_D \right\},$$

On the physical boundaries, we impose Dirichlet conditions according to the original equations (1). On the artificial subdomain boundaries, we assume both  $u = 0$  and  $p = 0$ . Similar boundary conditions were used in [38].

Let  $R_i^h : V_h \times P_h \rightarrow V_h^i \times P_h^i$  be a restriction operator, which returns all degrees of freedom (both velocity and pressure) associated with the subspace  $V_h^i \times P_h^i$ .  $R_i^h$  is a  $4n_i \times 4n$  matrix with values of either 0 or 1, where  $n$  and  $n_i$  are the total number of mesh points in  $\mathcal{T}^h$  and  $\mathcal{T}_i^{h,\delta}$ , respectively, and  $\sum_{i=1}^N 4n_i \geq 4n$ . Note that for  $P_1 - P_1$  elements, we have four variables per mesh point, three

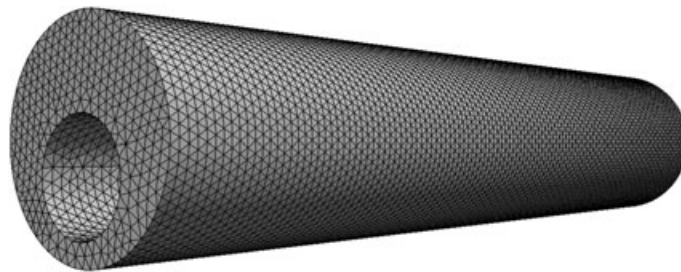


Figure 1. A sample 3D tetrahedron mesh.

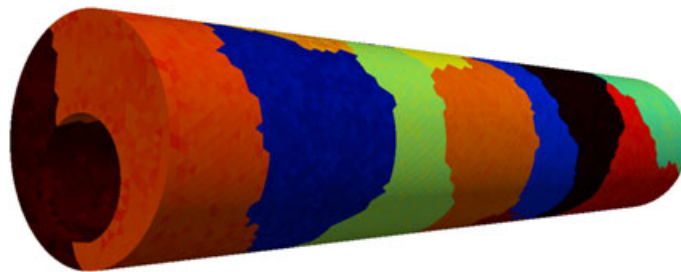


Figure 2. A sample domain decomposition with 16 subdomains; the elements with the same color belong to the same subdomain.

for the velocity and one for the pressure. Then, the extension operator  $(R_i^h)^T$  can be defined as the transpose of  $R_i^h$ . The multiplication of  $R_i^h$  (and  $(R_i^h)^T$ ) with a vector does not involve any arithmetic operation, but does involve communication in a distributed memory parallel implementation. Using the restriction matrix, we write the additive Schwarz preconditioner in the matrix form as

$$M_k^{-1} = \sum_{i=1}^N (R_i^h)^T J_i^{-1} R_i^h,$$

where  $J_i^{-1}$  is subspace inverse of  $J_i = R_i^h J (R_i^h)^T$ . We remark that the global-to-local restriction operator  $R_i^h$  collects the data from neighboring subdomains and the local-to-global prolongation operator  $(R_i^h)^T$  sends partial solution to neighboring subdomains.  $J_i^{-1}$  in  $M_k^{-1}$  often are solved by a sparse LU decomposition or an incomplete decomposition such as ILU with some levels of fill-ins [39].

### 3. NUMERICAL RESULTS AND DISCUSSION

In this section, we first provide a validation of the proposed discretization and solver using a test problem that has an analytic solution, and then we consider a non-Newtonian rotational eccentric annular flow problem to investigate the robustness and the parallel performance of the NKS algorithm. In addition, we discuss some interesting behavior of the flow based on the numerical experiments. In the last subsection, we study the non-Newtonian effect on the entrance length.

#### 3.1. Validation of the proposed discretization method

To validate the proposed stabilized finite element method for non-Newtonian flows, we consider a simple test case that has an analytical solution. This is a steady-state non-Newtonian power-law flow passing through a circular tube [40]. Specifically, a 3D cylindrical domain of length  $L = 5$  and radius  $R = 0.5$  is used. The unit uniform inlet velocity, the outlet stress-free, and the no-slip wall boundary conditions are imposed. The Reynolds number is defined as  $Re = \frac{\rho V_{in} R}{\mu}$ , based on the inlet velocity, and the radius as the characteristics of the velocity and length, respectively. Here, the parameters in Equation (2) are used for nonlinear viscosity: the density  $\rho = 1$  and the consistency index  $\mu_0 = 0.01$ , and the cutoff value  $\gamma_0 = 10^{-6}$ . The velocity profile near the inlet region is uniform, and the shape of the velocity profile is varied with respect to the axial axis (the flow is slower near the wall because of the viscous effect) until it is fully developed to be a parabolic type velocity. The analytical solution for the axial velocity profile in the cylindrical coordinates at some particular cross-section within the fully-developed region takes the following form,

$$\frac{V_z(r)}{V_{in}} = \frac{3n+1}{n+1} \left( 1 - \left( \frac{r}{R} \right)^{\left( \frac{n+1}{n} \right)} \right).$$

The detailed derivation of the analytical solution can be found in [4]. A sequence of uniform meshes ranging from about 30,000 elements for the coarsest mesh to 1,800,000 elements. To perform the mesh convergence analysis, we compute the discrete two-norm errors for different values of  $n$  and  $Re = 25$  with different mesh sizes, where the difference between the analytical and the numerical solutions is evaluated at the 100 equally spaced grid points along the diameter. As shown in Table I, quadratic or better convergence is achieved for all values of  $n$ .

From the analytical solution, we know that the velocity profile is independent of the values of Reynolds number, which is confirmed by the numerical results in Figure 3. For a fixed  $n$ , all the velocity profile curves corresponding to different  $Re$  coincide. As shown also in the same figure, the maximum of the outlet velocity profile is located at the center and its value increases as the power-law index,  $n$ , increases.

Table I. The discrete 2-norm error of the Galerkin/least squares finite element solutions with respect to the mesh size and their convergence rates for  $n = 0.5, 1.0, \text{ and } 1.5$ .

Meshes	$h_K$	# of nodes	$\ error_{n=1.0}\ _2$	$\ error_{n=0.5}\ _2$	$\ error_{n=1.5}\ _2$
		# of elements			
Mesh_A	0.1	5797	0.13424	0.26187	0.19397
		28780			
Mesh_B	0.08	10577	0.08820	0.13581	0.13384
		54211			
Mesh_C	0.05	36952	0.03128	0.03998	0.05624
		198218			
Mesh_D	0.02	323394	0.00528	0.00398	0.00811
		1800859			
Convergence rate			2.0	2.6	2.0

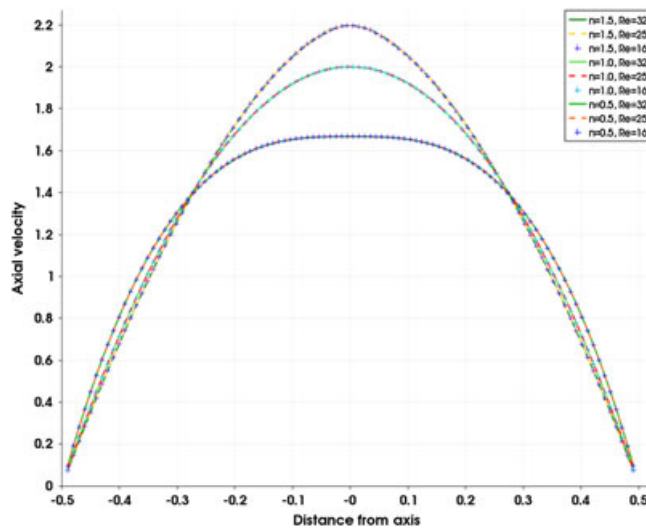


Figure 3. The velocity profile with different  $n$  and  $Re$ .

3.2. A rotational eccentric annular flow problem

To further study the numerical performance of the proposed algorithm, we consider a non-Newtonian rotational eccentric annular flow problem, which is described mathematically in Equation (1) defined in the computational domain  $\Omega$ ; see Figure 4 for the geometrical configuration of the flow problem and associate boundary conditions. The boundary consists of four segments:  $\Gamma = \Gamma_{in} \cup \Gamma_{out} \cup \Gamma_{wall\_in} \cup \Gamma_{wall\_out}$ . We apply a uniform velocity,  $u_{in}$ , on  $\Gamma_{in}$ ; a stress-free boundary condition on  $\Gamma_{out}$ ; a no-slip boundary condition on the walls; a stationary condition,  $u = 0$ , on  $\Gamma_{wall\_out}$ ; and a rotational condition,  $u = u_{rot}$ , on  $\Gamma_{wall\_in}$ . Figure 5 shows the geometric configuration for the circular cross-section of the eccentric annulus.  $R_I$  and  $R_O$  are the radii of these two cross-sections. The ratio of two radii is given in  $\kappa = R_I/R_O$ , and the eccentricity is defined as  $\varepsilon = e/(R_O - R_I)$ . In addition, the non-dimensional flow parameters are defined as follows

$$\text{Axial Reynolds number: } Re_z \equiv \frac{\rho u_{in} D_h}{\mu_F},$$

$$\text{Azimuthal Reynolds number: } Re_r \equiv \frac{\rho u_{rot} D_h}{\mu_F},$$

$$\text{Reynolds number ratio: } r_{Re} \equiv \frac{Re_z}{Re_r},$$

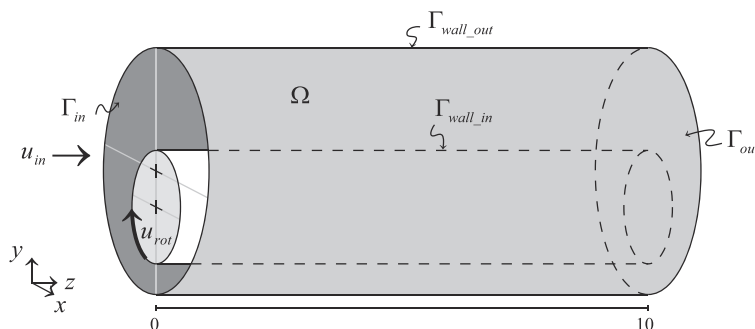


Figure 4. 3D rotational eccentric annulus geometry.

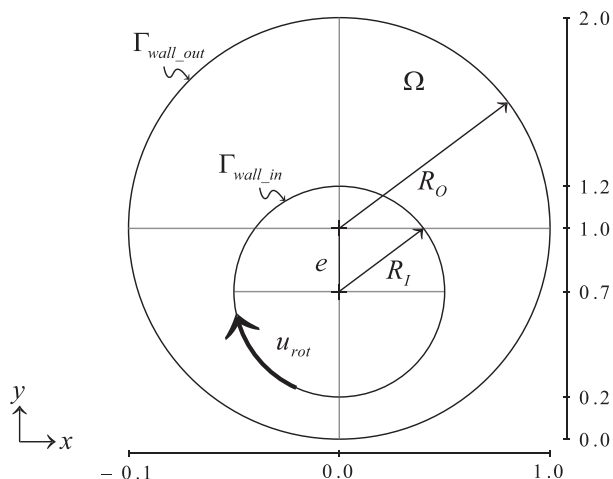


Figure 5. Schematic view of 3D rotational eccentric annulus cross section.

Table II. Parametric settings for four test cases.

$u_{in}$	$Re_z$	$u_{rot}$	$Re_r$	$rRe$
0.0	0	1.0	100	<b>0.0</b>
0.1	10	1.0	100	<b>0.1</b>
1.0	100	1.0	100	<b>1.0</b>
2.0	200	1.0	100	<b>2.0</b>

where  $D_h = 2(R_O - R_I)$  is the hydraulic diameter of eccentric annuli and  $\mu_F$  is the characteristic viscosity for the flow, defined as  $\mu_0 \left(\frac{u_{rot}}{D_h}\right)^{n-1}$ .

**Robustness and parallel performance of Newton–Krylov–Schwarz.** We study the robustness and the efficiency of the NKS algorithm with respect to the power-law index,  $n$ , and the Reynolds number ratio,  $rRe$ . Detailed parameter settings for the numerical experiments are listed in Table II. A zero initial guess is employed, when possible, and a power-law index-based continuation method is used to generate the initial guess for other test cases. We claim the convergence of the NKS algorithm when the absolute tolerance  $\|F(x^{(k)})\|_2 < 10^{-10}$  or the relative tolerance  $\|F(x^{(k)})\|_2 < 10^{-6}\|F(x^{(0)})\|_2$  is satisfied. The Jacobian system is solved inexactly by using an additive Schwarz preconditioned GMRES with forcing term,  $\eta_k = 10^{-4}$ . In the parallel implementation, each subdomain problem is assigned to a core and the subdomain linear system is solved by a sparse LU decomposition method. The overlapping size for the Schwarz preconditioner is set to be 1.

Table III shows the number of Newton iterations, the average number of GMRES iterations, and the timing results of each case. We summarize some of the observations as follows.

- For fixed  $r_{Re}$ , compared with the Newtonian case  $n = 1$ , the number of Newton iterations increases as the power-law index  $n$  increases ( $> n$ ) or decreases ( $< n$ ), in which the non-Newtonian effect is more significant. As shown in Figure 6, NKS converges quadratically for Newtonian flows, while for the cases of non-Newtonian flows, the rate of convergence of NKS degrades to linear.

Table III. Nonlinear and linear iteration counts and timing results.

$n$	$r_{Re} = 0.0$		$r_{Re} = 0.1$		$r_{Re} = 1.0$		$r_{Re} = 2.0$	
	$n_{New}$ ( $n_{GMRES}$ )	time(sec)						
0.5	25(70.1)	6778.5	18(73.3)	4815.5	17(82.4)	4608.8	15(92.9)*	4192.3*
0.6	21(72.1)	6810.9	17(72.2)	4391.6	14(83.3)	3463.1	12(86.7)*	2920.3*
0.75	19(72.4)	4951.2	15(71.9)	3707.3	10(83.0)	2583.1	11(84.2)	2836.5
0.8	17(71.3)	4306.8	15(71.7)	3829.2	9(80.3)	2381.3	10(83.9)	2513.9
1.0	7(63.3)	1595.9	6(67.8)	1313.8	5(81.0)	1332.0	8(78.1)	2101.8
1.2	15(72.3)	3849.4	13(71.2)	3214.3	9(76.8)	2345.5	10(78.3)	2460.8
1.25	15(72.3)	4137.7	13(71.5)	3054.9	10(75.2)	2443.9	10(81.7)	2640.2
1.4	15(71.7)	4512.8	13(70.8)	3256.0	14(67.6)	3407.3	15(76.7)	3856.6
1.5	17(72.8)	4545.9	22(40.9)	5666.5	32(42.8)	7845.4	19(79.9)	4945.1

' $n_{New}$ ' denotes the number of Newton iterations and ' $n_{GMRES}$ ' denotes the average number of generalized minimal residual method iterations per Newton iteration. The mark '\*' indicates that the parameter continuation method is used, where the converged solution with  $n = 0.75$  is used as an initial guess.

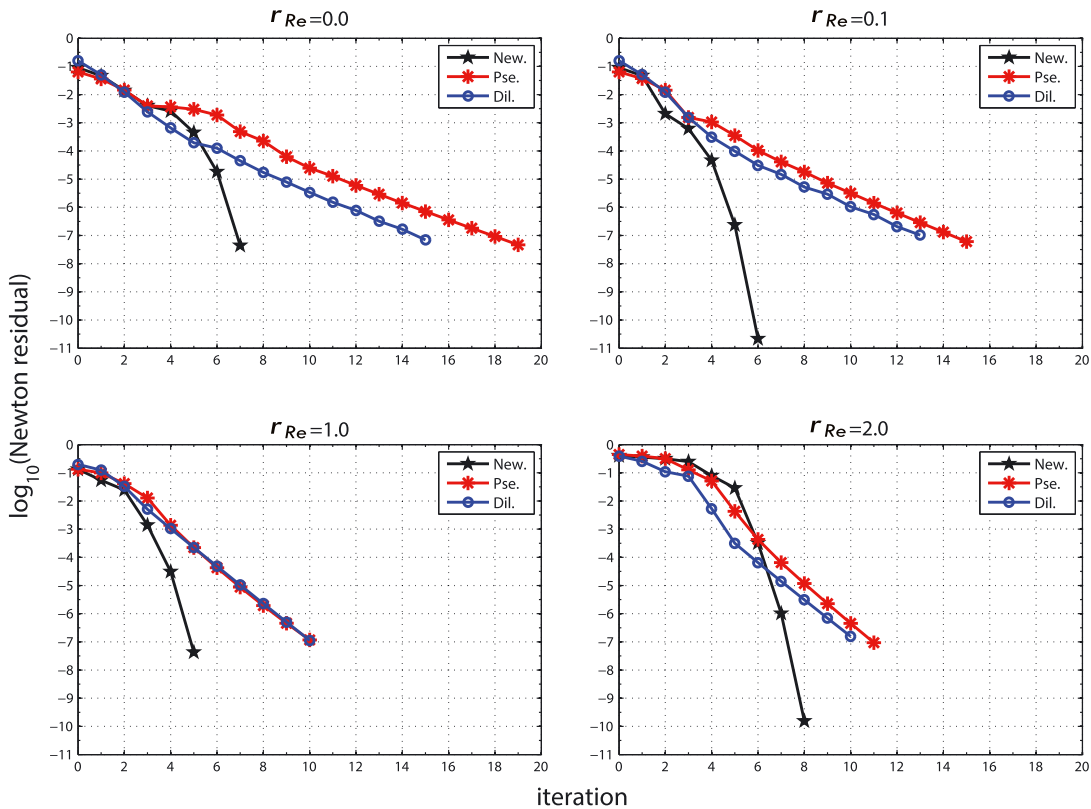


Figure 6. Histories of nonlinear residuals for different  $r_{Re}$ . Here, 'New.' is for Newtonian flows, 'Pse.' is for  $n = 0.75$  case, and 'Dil.' is for  $n = 1.25$  case.

- For fixed  $n$  ranging within  $[0.75, 1.4]$ , the number of Newton iterations decreases then increases as  $r_{Re}$  increases. At the beginning ( $r_{Re} = 0.0$ ), the flow is dominated by the nonlinear viscosity and at the end ( $r_{Re} = 2.0$ ), the flow is dominated by the nonlinear convection.
- When both the nonlinear viscosity and convection effect are strong (e.g.,  $n$  is close to 0.5 and  $r_{Re}$  is close to 2.0), NKS fails to converge when zero initial guess is used. Hence, in addition to the globalization linesearch technique, we use a power-law index based continuation method to generate the initial guess. More precisely speaking, we first solve the flow problem with  $n = 0.75$ , then its converged solution is used as an initial guess for the cases of  $n = 0.5$  and 0.6.

The parallel performance of 3D rotational eccentric annular flows for cases with different  $r_{Re}$  are shown in Table IV. It is clear that for fixed  $r_{Re}$ , our fluid solver is nonlinearly scalable and the average number of GMRES iterations increases mildly as the number of processors grows. In terms of the total computing time, our parallel fluid solver achieves a good scalability with up to 512 processors. Generally speaking, the computational cost for the pseudoplastic and dilatant cases is two to three times more expensive than the Newtonian case mainly because of the fact that more Newton iterations is needed. This is an indication that non-Newtonian flows are more nonlinear than Newtonian flows.

**Some quantitative analysis of the flows.** Figures 7 and 8 show the viscosity distribution and shear stress distribution for the cases of pseudoplastic ( $n = 0.5$ ) and dilatant ( $n = 1.5$ ) flows. The relationship between viscosity and shear stress is as expected. The shear stress for the pseudoplastic case decreases as the viscosity increases, and the shear stress for the dilatant case increases as the viscosity increases. We also present plots of other physical quantities of the flows, including the pressure distribution (Figure 9), the velocity distribution (Figure 10), and the streamlines (Figure 11). For each case, we compare the effect on the values of different power-law index  $n$  under the same flow boundary conditions. Some observations are made as follows:

- The distributions of the pressure gradient of all cases are similar, and the only significant difference appears at the inlet near the inner cylinder for the dilatant cases ( $n = 1.25$  and 1.5).

Table IV. Parallel performance of Newton–Krylov–Schwarz.

$r_{Re}$	$np$	Newtonian		pseudoplastic		dilatant	
		$n_{New}(n_{GMRES})$	time(sec)	$n_{New}(n_{GMRES})$	time(sec)	$n_{New}(n_{GMRES})$	time(sec)
0.0	64	7(63.3)	1595.9	19(72.4)	4951.2	15(72.3)	4137.7
	128	7(78.9)	622.0	19(92.2)	2259.9	15(90.5)	1680.3
	256	7(105.0)	249.5	19(122.1)	825.4	15(121.1)	626.3
	512	7(132.2)	101.2	19(150.9)	316.3	15(150.5)	261.5
0.1	64	6(67.8)	1313.8	15(71.9)	3707.3	13(71.5)	3054.9
	128	6(84.1)	617.3	16(89.9)	1855.0	13(89.7)	1445.9
	256	6(113.7)	193.5	16(120.1)	620.1	13(119.2)	547.0
	512	6(139.5)	96.1	16(149.4)	252.1	13(148.6)	210.9
1.0	64	5(81.0)	1332	10(83.0)	2583.1	10(75.2)	2443.9
	128	5(102.4)	448.8	10(103.3)	1045.5	10(95.2)	1021.9
	256	5(134.8)	207.5	10(136.7)	402.0	10(122.8)	382.6
	512	5(165.6)	81.5	10(168.8)	177.1	10(153.4)	164.4
2.0	64	8(78.1)	2101.8	11(84.2)	2836.5	10(81.7)	2640.2
	128	8(99.0)	725.7	11(107.2)	1196.9	10(103.4)	921.0
	256	8(129.9)	267.8	11(137.8)	515.8	10(135.8)	434.8
	512	8(162.5)	125.1	11(175.1)	199.1	10(167.2)	170.6

‘ $n_{New}$ ’ denotes the number of Newton iterations and ‘ $n_{GMRES}$ ’ denotes the average number of generalized minimal residual method iterations per Newton iteration.

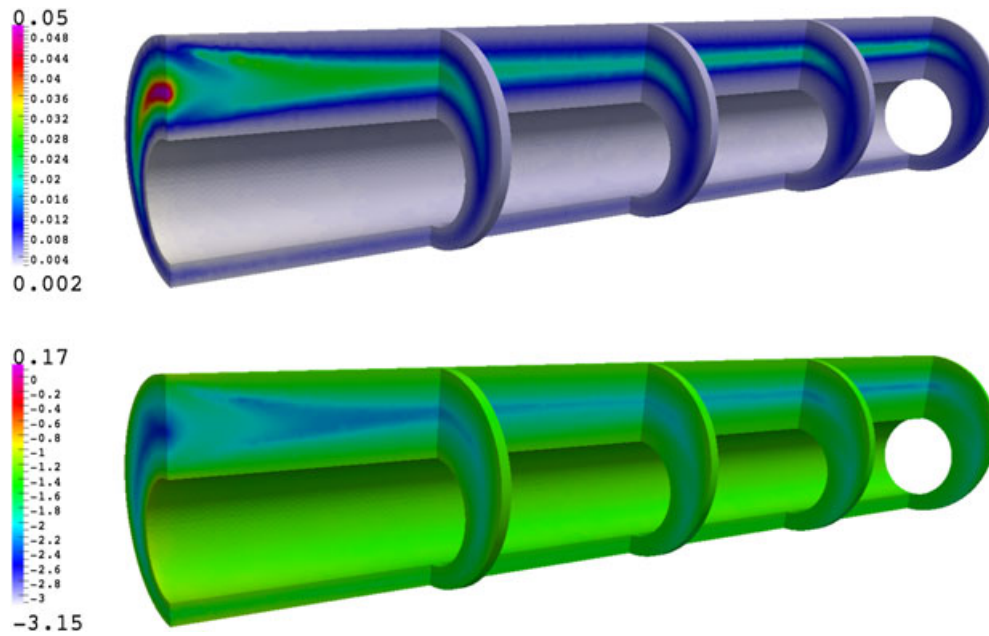


Figure 7. A comparison of viscosity (top) and shear stress in the logarithmic scale (bottom) for the case of pseudoplastic ( $n = 0.5$ ).

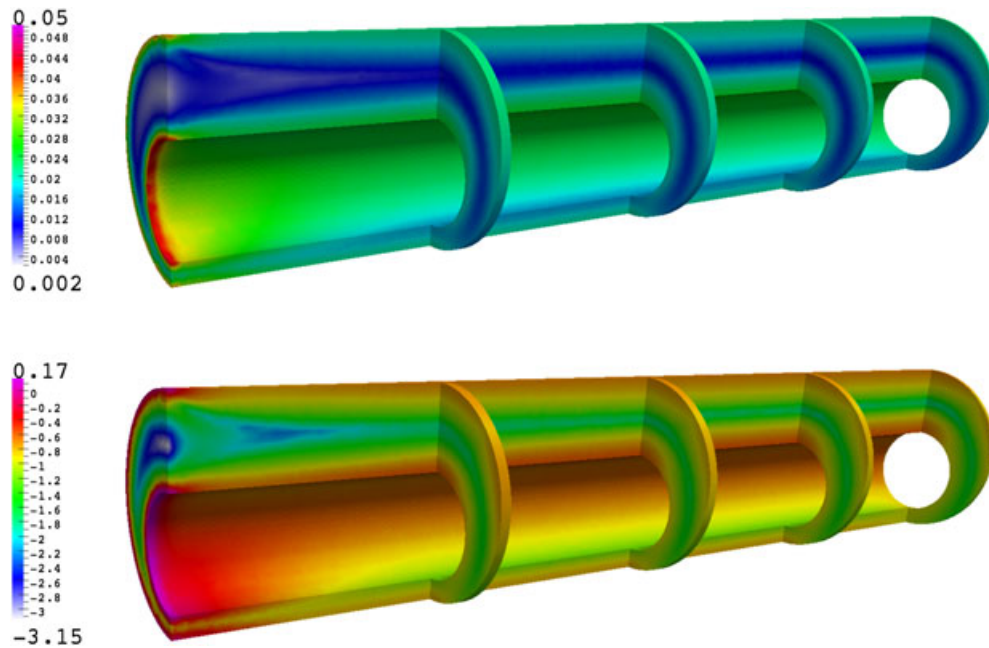


Figure 8. A comparison of viscosity (top) and shear stress in the logarithmic scale (bottom) for the case of dilatant ( $n = 1.5$ ).

- For the velocity distribution, as the power-law index decreases, the corresponding flow becomes slower when fully developed.
- All cases have three similar major patterns in the streamlines: straight streamlines in the top gap, rotational streamlines near the inner-cylinder, and helical streamlines between the inner and outer cylinders. However, as the value of  $n$  becomes smaller, the helical streamlines near the sides disappear.

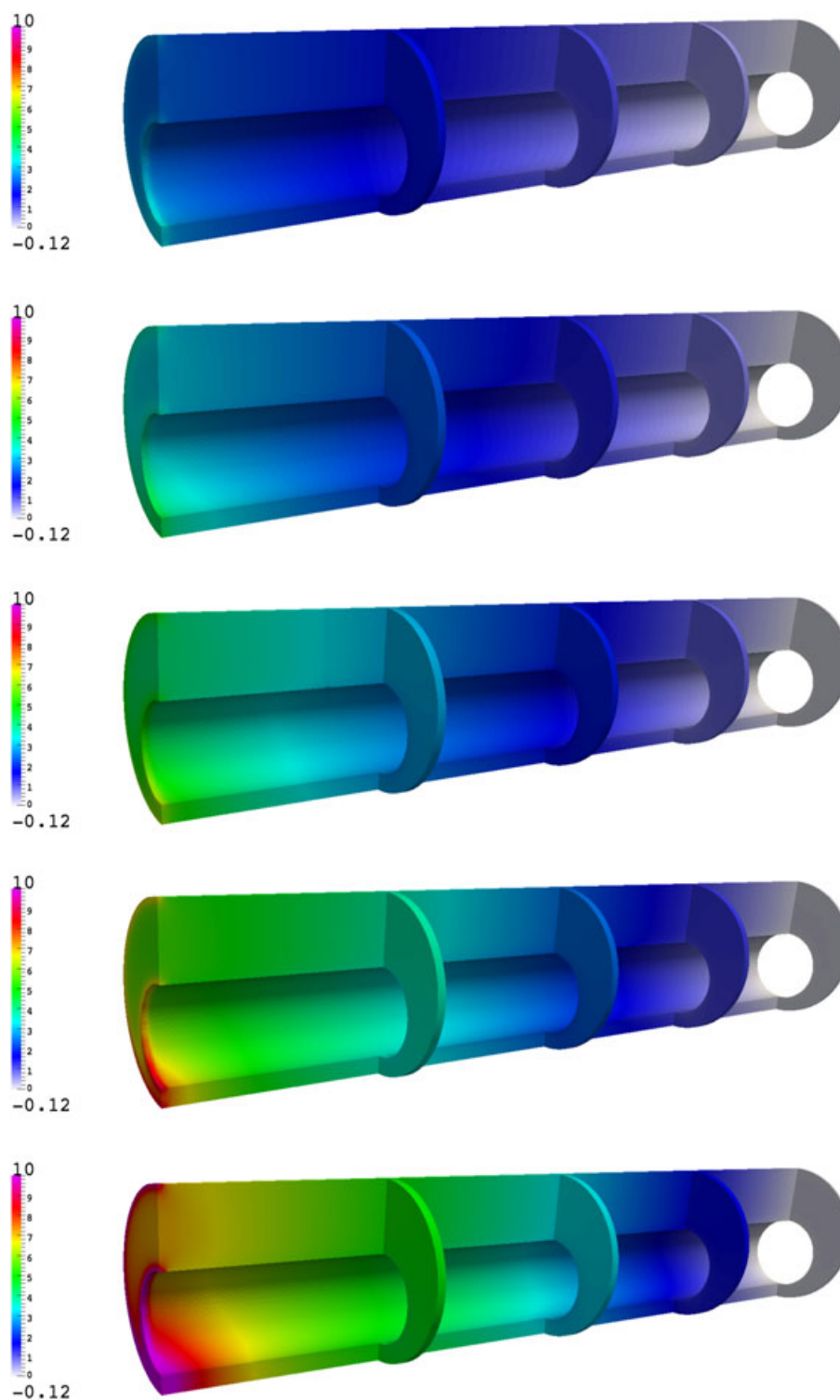


Figure 9. Pressure distributions for the cases with different values of the power-law index in the order of  $n = 0.50, 0.75, 1.0, 1.25,$  and  $1.50$ .

**Non-Newtonian effect on the entrance length.** The flow is referred to as fully developed when the velocity profile remains unchanged at any cross section of the flow domain. As the fluid enters and flows through the annulus, the viscosity causes the fluid to stick to the walls (the no-slip

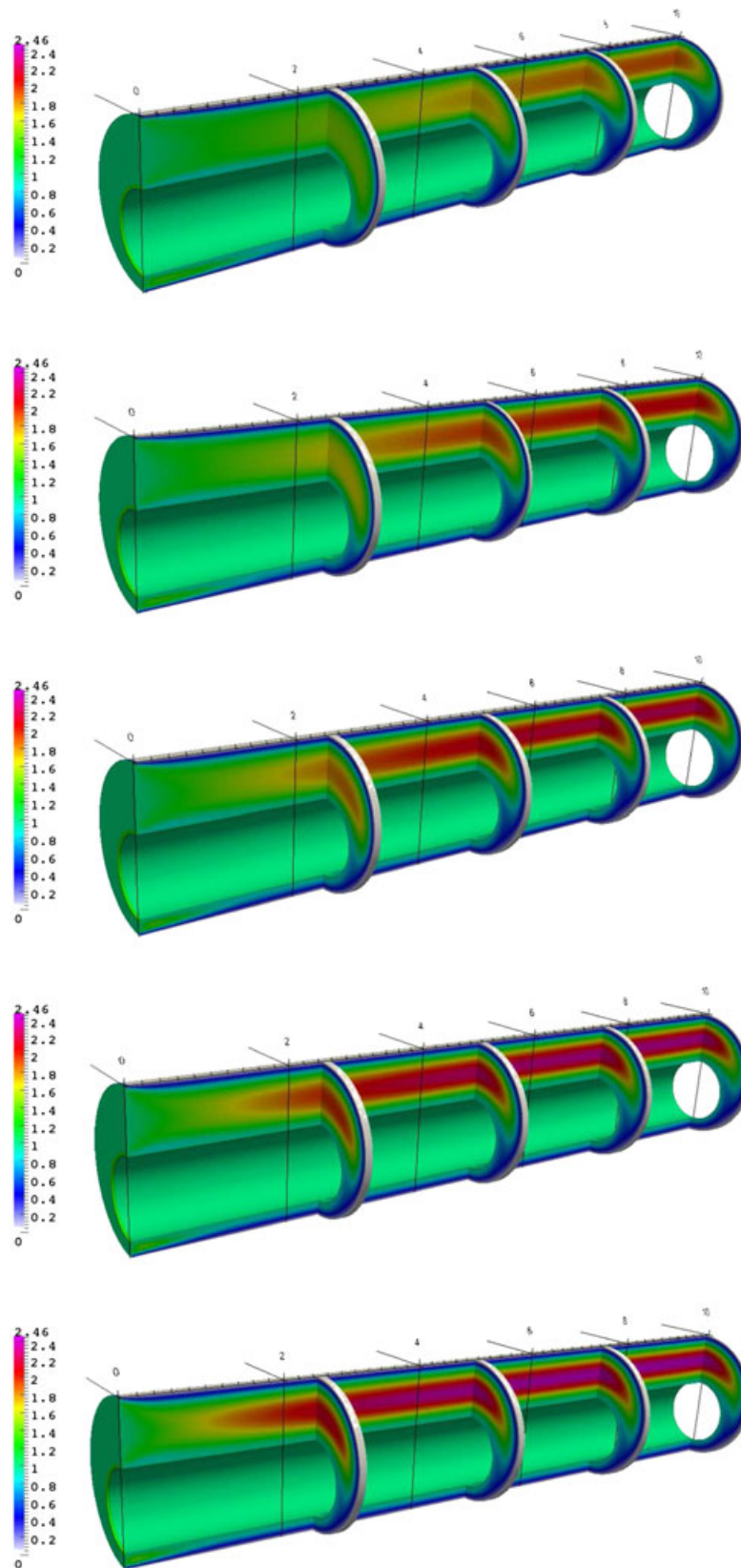


Figure 10. Velocity distributions for the cases with different values of the power-law index in the order of  $n = 0.50, 0.75, 1.0, 1.25,$  and  $1.50$ .

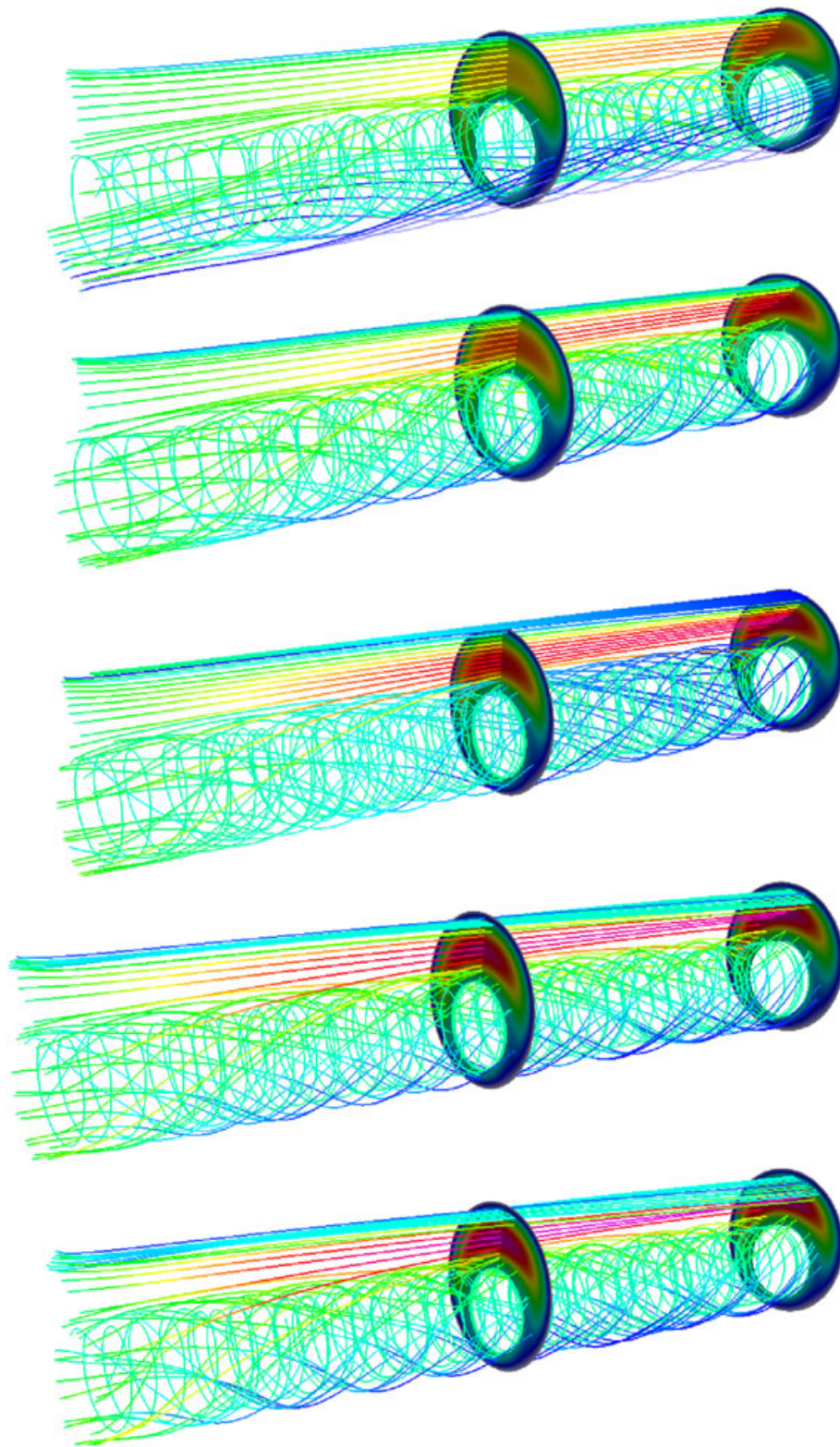


Figure 11. Streamlines for the cases with different values of the power-law index in the order of  $n = 0.50, 0.75, 1.0, 1.25,$  and  $1.50$ .

boundary condition). Because of the viscous effect, the boundary layer starts to grow, such that the initial velocity profile changes along the annulus until the fluid reaches certain points where the velocity profile does not vary with the axial position. The distance from the entrance to that point is called the entrance length,  $l_e/D_h$ . Here, the distance  $l_e$  is normalized by the hydraulic diameter of the eccentric annuli  $D_h$ . We are interested in finding the relationship between the entrance length  $l_e/D_h$  [41], the power-law index  $n$ , and the Reynolds number ratio  $r_{Re}$  for rotational eccentric annulus flows.

We first consider four different axial velocities or four different Reynolds number ratios as listed in Table II for the pseudoplastic fluid with  $n = 0.75$  and the dilatant fluid with  $n = 1.25$ . Figures 12–15 show the comparison of velocity contour plots on the  $yz$ -plane with different inflow axial velocities for Newtonian, pseudoplastic, and dilatant fluids. In the case of  $r_{Re} = 0.0$  and  $r_{Re} = 0.1$ , because the rotational force is much stronger than the pressure gradient, the fluid flows are never fully developed, and on the other hand, in the case of  $r_{Re} = 1.0$  and  $r_{Re} = 2.0$ , three types of fluids are all fully developed at certain points.



Figure 12.  $r_{Re} = 0.0$  velocity profiles of (a) Newtonian fluid, (b) pseudoplastic fluid, and (c) dilatant fluid.

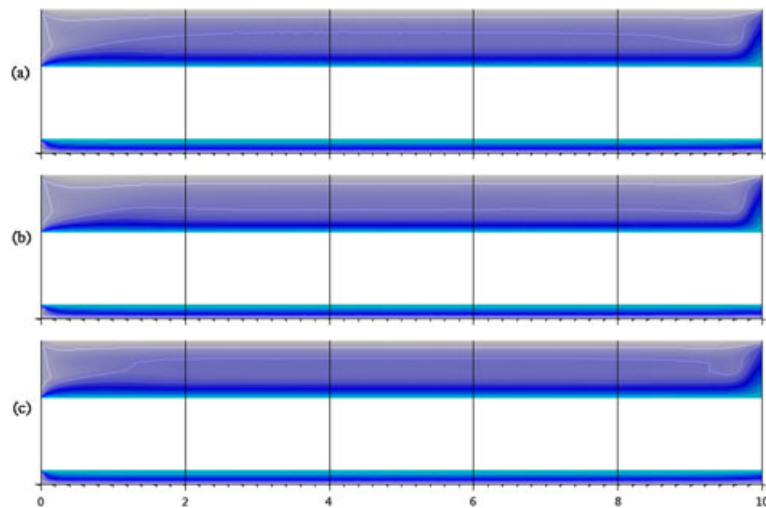


Figure 13.  $r_{Re} = 0.1$  velocity profiles of (a) Newtonian fluid, (b) pseudoplastic fluid, and (c) dilatant fluid.

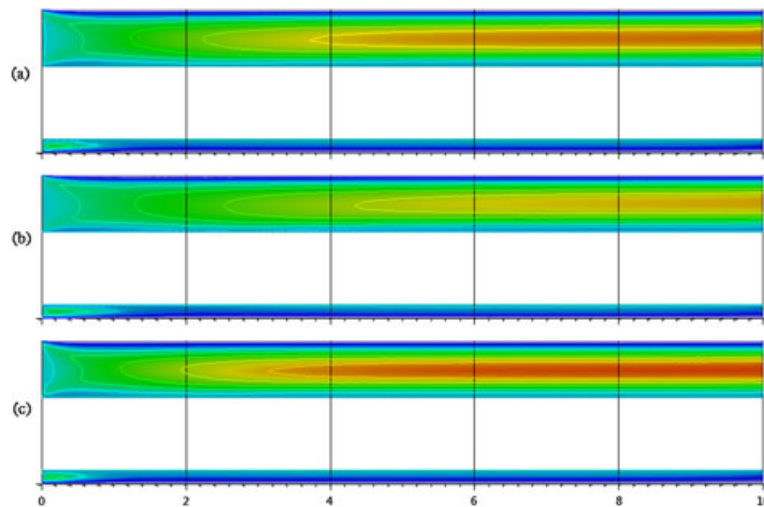


Figure 14.  $r_{Re} = 1.0$  velocity profiles of (a) Newtonian fluid, (b) pseudoplastic fluid, and (c) dilatant fluid.

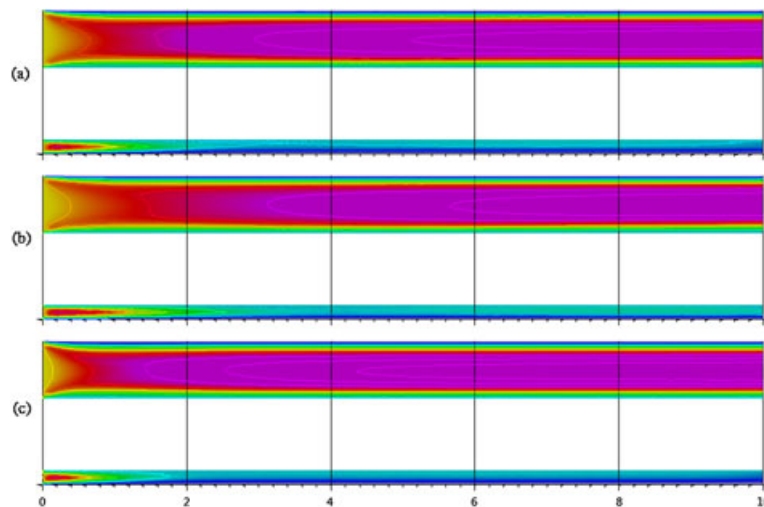


Figure 15.  $r_{Re} = 2.0$  velocity profiles of (a) Newtonian fluid, (b) pseudoplastic fluid, and (c) dilatant fluid.

Table V. The entrance length  $l_e/D_h$ .

$r_{Re}$	pseudoplastic	Newtonian	dilatant
1.0	7.4	6.6	5.8
2.0	8.2	7.8	6.8

The entrance lengths for different kinds of fluids and Reynolds number ratios are summarized in Table V. For the case of  $r_{Re} = 1.0$  fully developed conditions occur at about  $z = 7.4$ ,  $z = 6.6$  and  $z = 5.8$  for pseudoplastic fluid, Newtonian fluid and dilatant fluid, respectively. And for the case of  $r_{Re} = 2.0$  fully developed conditions occur at about  $z = 8.2$ ,  $z = 7.8$  and  $z = 6.8$  for pseudoplastic fluid, Newtonian fluid and dilatant fluid, respectively. Therefore, the entrance length of the dilatant fluid ( $n > 1$ ) is shorter than that of the Newtonian fluid, and the pseudoplastic fluid ( $n < 1$ ) has the shortest entrance length. Moreover, the smaller the Reynolds number ratio is, the shorter the entrance length is.

## 4. CONCLUSIONS

We introduced a stabilized finite element method for 3D non-Newtonian fluids and a corresponding parallel NKS algorithm for solving the large, sparse, highly nonlinear system of equations arising from the finite element discretization. The finite element method was carefully validated by comparing its solution with an analytical solution that is available for a special test problem. We observed that NKS works well in most cases for different power-law index and the Reynolds number ratio; more precisely, NKS converges quadratically for Newtonian flows, but as the power-law index moves away from 1.0 (i.e., the non-Newtonian effect increases), the convergence changes toward linear. When both the nonlinear viscosity and the nonlinear convection are strong, standard NKS with zero initial guess fails to converge. In such situations, we introduced a power-law index-based continuation method that generates an initial guess for NKS using the solution of a flow problem corresponding to a power-law index closer to 1.0. With this technique, we are able to solve problems with a wide range of power-law index values and Reynolds number ratios. Moreover, using the computational results, we provided some quantitative analysis of the 3D flows in terms of streamlines, pressure distributions, and shear stress distributions. We also demonstrated that the domain decomposition-based preconditioning algorithm is quite effective for these rather difficult, highly ill-conditioned systems of algebraic equations. Superlinear speedup is obtained with up to 512 processors. In this work, we focused on how the performance of NKS is affected by the physical parameters, including the Reynolds number and the power-law indices, and so on. The convergence rate of the linear iterative solver may be further improved by tuning some of the parameters in the Schwarz preconditioners, some parametric studies for several closely related problems can be found in [24, 42]. In the future, we plan to continue to work on more complicated non-Newtonian fluids such as Bingham fluid and time-dependent fluids. Finally, our algorithmic framework is quite general and can be extended to other cases with complex geometry and fluid conditions.

## ACKNOWLEDGEMENTS

We are grateful to the National Center for High-performance Computing in Taiwan for computer time and facilities. The first two authors were supported in part by the Ministry of Science and Technology of Taiwan, MOST 102-2115-M-008-013 and the last author was supported in part by NSF, CCF-1216314. The research was supported in part by 863 project 2015AA01A302, NSFC 91330111, and Shenzhen KQCX20130628112914303.

## REFERENCES

1. Bird RB, Armstrong RC, Hassager O. *Dynamics of Polymeric Liquids, Vol 1: Fluid Mechanics*. John Wiley and Sons: New York, 1987.
2. Brujan E. *Cavitation in Non-Newtonian Fluids: With Biomedical and Bioengineering Applications*. Springer: Heidelberg, 2011.
3. Owens RG, Phillips TN. *Computational Rheology*. Imperial College Press: London, 2002.
4. Chhabra RP, Richardson JF. *Non-Newtonian Flow and Applied Rheology: Engineering Applications*. Elsevier: Amsterdam, 2011.
5. Carey GF, Wang KC, Joubert WD. Performance of iterative methods for Newtonian and generalized Newtonian flows. *International Journal for Numerical Methods in Fluids* 1989; **9**:127–150.
6. Grillet AM, Yang B, Khomami B, Shaqfeh E SG. Modeling of viscoelastic lid driven cavity flow using finite element simulations. *Journal of Non-Newtonian Fluid Mechanics* 1999; **88**:99–131.
7. Mitsoulis E, Zisis Th. Flow of Bingham plastics in a lid-driven square cavity. *Journal of Non-Newtonian Fluid Mechanics* 2001; **101**:173–180.
8. Dean EJ, Glowinski R, Guidoboni G. On the numerical simulation of Bingham visco-plastic flow: old and new results. *Journal of Non-Newtonian Fluid Mechanics* 2007; **142**(1):36–62.
9. Elias RN, Martins M AD, Coutinho ALGA. Parallel edge-based solution of viscoplastic flows with the SUPG/PSPG formulation. *Computational Mechanics* 2005; **38**:365–381.
10. Elias RN, Coutinho ALGA, Martins MAD. Inexact Newton-type methods for the solution of steady incompressible viscoplastic flows with the SUPG/PSPG finite element formulation. *Computer Methods in Applied Mechanics and Engineering* 2006; **195**:3145–3167.
11. Eisenstat SC, Walker HF. Choosing the forcing terms in inexact Newton method. *SIAM Journal on Scientific Computing* 1996; **17**:16–32.

12. Nejat A, Jalain A, Sharbatdar M. A Newton-Krylov finite volume algorithm for the power-law non-Newtonian fluid flow using pseudo-compressibility technique. *Journal of Non-Newtonian Fluid Mechanics* 2011; **166**:1158–1172.
13. Sahin M, Wilson H. A semi-staggered dilation-free finite volume method for numerical solution of viscoelastic fluid flows on all-hexahedral elements. *Journal of Non-Newtonian Fluid Mechanics* 2007; **147**:79–91.
14. Sahin M. A stable unstructured finite volume method for parallel large-scale viscoelastic fluid flow calculations. *Journal of Non-Newtonian Fluid Mechanics* 2011; **166**:779–791.
15. Grinevich PP, Olshanskii MA. An iterative method for the Stokes-type problem with variable viscosity. *SIAM Journal on Scientific Computing* 2009; **31**:3959–3978.
16. Gwynnlyw DRh, Phillips TN. Preconditioned iterative methods for unsteady non-Newtonian flow between eccentrically rotating cylinders. *SIAM Journal on Scientific Computing* 1996; **17**:1369–1394.
17. Dennis JE, Schnabel RB. *Numerical Methods for Unconstrained Optimization and Nonlinear Equations*. SIAM: Philadelphia, 1996.
18. Smith BF, Bjørstad PE, Gropp W. *Domain Decomposition: Parallel Multilevel Methods for Elliptic Partial Differential Equations*. Cambridge University Press: Cambridge, 1996.
19. Wu Y, Cai X-C. A fully implicit domain decomposition based ALE framework for three-dimensional fluid-structure interaction with application in blood flow computation. *Journal of Computational Physics* 2014; **258**:524–537.
20. Wu Y, Cai X-C. A parallel two-level method for simulating blood flows in branching arteries with the resistive boundary condition. *Computers & Fluids* 2011; **45**:92–102.
21. Barker A, Cai X-C. Two-level Newton and hybrid Schwarz preconditioners for fluid-structure interaction. *SIAM Journal on Scientific Computing* 2010; **32**:2395–2417.
22. Barker A, Cai X-C. Scalable parallel methods for monolithic coupling in fluid-structure interaction with application to blood flow modeling. *Journal of Computational Physics* 2010; **229**:642–659.
23. Cai X-C, Gropp WD, Keyes DE, Melvin RG, Young DP. Parallel Newton-Krylov-Schwarz algorithms for the transonic full potential equation. *SIAM Journal on Scientific Computing* 1998; **19**:246–265.
24. Hwang F-N, Wu C-Y, Cai X-C. Numerical simulation of three-dimensional blood flows using domain decomposition method on parallel computer. *Journal of the Chinese Society of Mechanical Engineers* 2010; **31**:199–208.
25. Prudencio EE, Byrd R, Cai X-C. Parallel full space SQP Lagrange-Newton-Krylov-Schwarz algorithms for PDE-constrained optimization problems. *SIAM Journal on Scientific Computing* 2006; **27**:1305–1328.
26. Escudier MP, Oliveira PJ, Pinho FT. Fully developed laminar flow of purely viscous non-Newtonian liquids through annuli including the effects of eccentricity and inner-cylinder rotation. *International Journal of Heat and Fluid Flow* 2002; **23**:52–73.
27. Chin WC. *Computational Rheology for Pipeline and Annular Flow*. Elsevier: Amsterdam, 2001.
28. Fang P, Manglik RM, Jog MA. Characteristics of laminar viscous shear-thinning fluid flows in eccentric annular channels. *Journal of Non-Newtonian Fluid Mechanics* 1999; **84**:1–17.
29. Manglik RM, Fang P. Effect of eccentricity and thermal boundary conditions on laminar fully developed flow in annular ducts. *International Journal of Heat and Fluid Flow* 1995; **16**:298–306.
30. Escudier MP, Gouldson IW, Oliveira PJ, Pinho FT. Effects of inner cylinder rotation on laminar flow of a Newtonian fluid through an eccentric annulus. *International Journal of Heat and Fluid Flow* 2000; **21**:92–103.
31. Wan S, Morrison D, Bryden IG. The flow of Newtonian and inelastic non-Newtonian fluids in eccentric annuli with inner-cylinder rotation. *Theoretical and Computational Fluid Dynamics* 2000; **13**:349–359.
32. Reddy JN, Gartling DK. *The Finite Element Method in Heat Transfer and Fluid Dynamics*. CRC press: Boca Raton, 2001.
33. Hughes TJR. *The Finite Element Method: Linear Static and Dynamic Finite Element Analysis*. Dover Publications: New York, 2000.
34. Franca LP, Frey SL. Stabilized finite element methods. II: the incompressible Navier-Stokes equations. *Computer Methods in Applied Mechanics and Engineering* 1992; **99**:209–233.
35. Saad Y, Schultz MH. GMRES: A generalized minimal residual algorithm for solving nonsymmetric linear systems. *SIAM Journal on Scientific and Statistical Computing* 1986; **7**(3):856–869.
36. Balay S, Brown J, Buschelman K, Gropp WD, Kaushik D, Knepley MG, McInnes LC, Smith BF, Zhang H. PETSc web page, 2014. Available from: <http://www.mcs.anl.gov/petsc>.
37. Nocedal J, Wright SJ. *Numerical Optimization*. Springer: New York, 1999.
38. Klawonn A, Pavarino LP. Overlapping Schwarz methods for mixed linear elasticity and Stokes problems. *Computer Methods in Applied Mechanics and Engineering* 1998; **165**:233–245.
39. Saad Y. *Iterative Methods for Sparse Linear Systems*. SIAM: Philadelphia, 2003.
40. Chhabra RP, Richardson JF. *Non-Newtonian Flow and Applied Rheology: Engineering Applications*, Vol. 195. Elsevier: Amsterdam, 2008.
41. Munson BR, Young DF, Okiishi TH, Huebsch WW. *Fundamentals of Fluid Mechanics*. John Wiley & Sons: New York, 2010.
42. Hwang F-N, Cai X-C, Cheng Y-L, Tsao C-W. A parallel fully coupled implicit domain decomposition method for numerical simulation of microfluidic mixing in 3D. *International Journal of Computer Mathematics* 2013; **90**: 615–629.